Article

Electrical mutual switching in a noncollinear-antiferromagnetic–ferromagnetic heterostructure

Ju-Young Yoon [1,2], Yutaro Takeuchi [1,3,4], Ryota Takechi[1,2], Jiahao Han [1,5] ✉, Tomohiro Uchimura [1,2], Yuta Yamane [1,6], Shun Kanai[1,2,4,5,7,8,9], Jun'ichi Ieda [10], Hideo Ohno [1,2,5,8,11] & Shunsuke Fukami [1,2,5,8,11,12] ✉

Spin-orbit torque (SOT) provides a promising mechanism for electrically encoding information in magnetic states. Unlike existing schemes, where the SOT is passively determined by the material and device structures, an active manipulation of the intrinsic SOT polarity would allow for flexibly programmable SOT devices. Achieving this requires electrical control of the current-induced spin polarization of the spin source. Here we demonstrate a proof-of-concept current-programmed SOT device. Using a noncollinear-anti-ferromagnetic/nonmagnetic/ferromagnetic Mn_3Sn/Mo/CoFeB hetero-structure at zero magnetic field, we show current-induced switching in the CoFeB layer due to the spin current polarized by the magnetic structure of the Mn_3Sn; by properly tuning the driving current, the spin current from the CoFeB further reverses the magnetic orientation of the Mn_3Sn, which deter-mines the polarity of the subsequent switching of the CoFeB. This scheme of mutual switching can be achieved in a spin-valve-like simple protocol because each magnetic layer serves as a reversible spin source and target magnetic electrode. It yields intriguing proof-of-concept functionalities for unconven-tional logic and neuromorphic computing.

The electrical control of magnetic states is the foundation of magnetic memory, logic, and computing. The spin-orbit torque (SOT), arising from the spin current produced by an electric current via spin-orbit interactions, offers an efficient approach for controlling the magnetic states[1–5]. In the conventional scenario that has been used in integrated-circuit demonstrations of non-volatile memory[6], the scheme of SOT switching is fixed by the material and device structures[5]. Moving for-ward, an effective manipulation over the polarity of SOT switching (clockwise or counter-clockwise under a fixed direction of electric current) can stimulate rich opportunities for information processing beyond the binary data storage. In the existing studies, such a task requires external control panels, such as preset[7–9] or persistent mag-netic fields[10,11] and strains from piezoelectric substrates[12–15]. These non-electric-current components bring additional complexity to the implementation of SOT devices. Given that the basic elements of SOT are just a magnetic heterostructure and an electric current[5], it should

[1]Laboratory for Nanoelectronics and Spintronics, Research Institute of Electrical Communication, Tohoku University, Sendai, Japan. [2]Graduate School of Engineering, Tohoku University, Sendai, Japan. [3]International Center for Young Scientists, National Institute for Materials Science, Tsukuba, Japan. [4]PRESTO, Japan Science and Technology Agency, Kawaguchi, Japan. [5]Advanced Institute for Materials Research, Tohoku University, Sendai, Japan. [6]Frontier Research Institute for Interdisciplinary Sciences, Tohoku University, Sendai, Japan. [7]Division for the Establishment of Frontier Sciences of Organization for Advanced Studies at Tohoku University, Tohoku University, Sendai, Japan. [8]Center for Science and Innovation in Spintronics, Tohoku University, Sendai, Japan. [9]National Institute for Quantum Science and Technology, Takasaki, Japan. [10]Advanced Science Research Center, Japan Atomic Energy Agency, Tokai, Japan. [11]Center for Innovative Integrated Electronic Systems, Tohoku University, Sendai, Japan. [12]Inamori Research Institute for Science, Kyoto, Japan. ✉e-mail: jiahao.han.c8@tohoku.ac.jp; s-fukami@riec.tohoku.ac.jp

in principle be possible to reverse the intrinsic SOT polarity by only programming the electric current in a simple protocol without the assistance of magnetic fields. This goal is of fundamental and practical significance because it represents a thorough exploitation of the interactions between the internal magnetic and electronic structures, which will enable new schemes of SOT switching and flexibly programmable devices that advance the current logic and computing technologies.

To achieve electric current control of the intrinsic SOT polarity, a spin source owning tunable signs of the charge-spin conversion is necessary. A potential solution arises from the magnetic spin Hall effect[16] (MSHE) and the resultant magnetic spin Hall torque[17–19] (MSHT) in noncollinear antiferromagnets (NCAFMs) with chiral-spin structures[20–22]. $D0_{19}$-Mn$_3$Sn (Fig. 1a) is a representative NCAFM exhibiting the MSHE, that is, the current-induced non-equilibrium spins are reversible upon flipping the chiral-spin structure of Mn$_3$Sn (ref. 16). The MSHE makes the field-free switching of perpendicular magnetization possible due to the out-of-plane polarization of the non-equilibrium spins[16–19,23,24]. Nevertheless, there remains a major obstacle towards the electric-current control of the MSHE, because the mechanism to achieve field-free switching of the magnetic spin source is still missing.

In this work, we demonstrate electrical mutual switching between the NCAFM Mn$_3$Sn and a ferromagnet (FM) CoFeB, that is, each magnetic layer works as both a reversible spin source and a target magnetic electrode. To be specific, CoFeB with a perpendicular magnetic easy axis undergoes field-free switching induced by the MSHT from Mn$_3$Sn, while Mn$_3$Sn with in-plane magnetic anisotropy can be switched by the spin current from CoFeB, also without external magnetic fields (Fig. 1b). The switching conditions of CoFeB and Mn$_3$Sn are separated in different regimes of electric current. In contrast to previous studies

that rely on external tuning knobs beyond a magnetic heterostructure and a current[7–15], our mutual switching exclusively implements interplay between the spin current and the magnetic structures of the FM and the NCAFM, thus leading to a switching protocol as succinct as a spin valve[25]. We further demonstrate a function of electrical turning on/off for the switching process and polarity-programmable memristive behaviors that arise from the multistep switching of Mn$_3$Sn. These functionalities open up new opportunities that cannot be achieved by conventional SOT switching[7–15,18,23,26,27] for logic and neuromorphic computing.

Results and discussion

Basic structural, transport, and magnetic properties

Figure 1b illustrates a noncollinear-antiferromagnetic/nonmagnetic/ferromagnetic Mn$_3$Sn/Mo/CoFeB heterostructure and the mechanism of the electrical mutual switching between Mn$_3$Sn and CoFeB. We prepare Ru(2 nm)/Mn$_3$Sn(17 nm)/Mo(t_{Mo})/CoFeB(1 nm)/MgO(1.3 nm)/TaO$_x$(1 nm) stacks on MgO(111) substrates (see Methods), where CoFeB has a perpendicular magnetic easy axis[28] and Mn$_3$Sn shows a magnetic easy plane lying in the film plane[29]. A Mo layer with a thickness of t_{Mo} is inserted between Mn$_3$Sn and CoFeB for magnetic separation. The (0001) orientation of Mn$_3$Sn is chosen to produce z-component spins[16,17] for the field-free switching of CoFeB. We measure the X-ray diffraction to characterize the crystal structure of Mn$_3$Sn. Only the (0002) and (0004) peaks of Mn$_3$Sn are observed in the 2θ-θ scan (Fig. 1c), indicating that the (0001) kagome plane is formed in the film plane. Moreover, the 60°-periodic Mn$_3$Sn(20$\bar{2}$1) peaks in the φ scan (Supplementary Fig. 1) confirm the fully epitaxial growth with the relationship of MgO(111)[1$\bar{1}$0] ∥Mn$_3$Sn(0001)[11$\bar{2}$0]. We note that Mn$_3$Sn has a chiral-spin structure with a weak net magnetization due to the distorted magnetic moments of the Mn atoms from a perfect
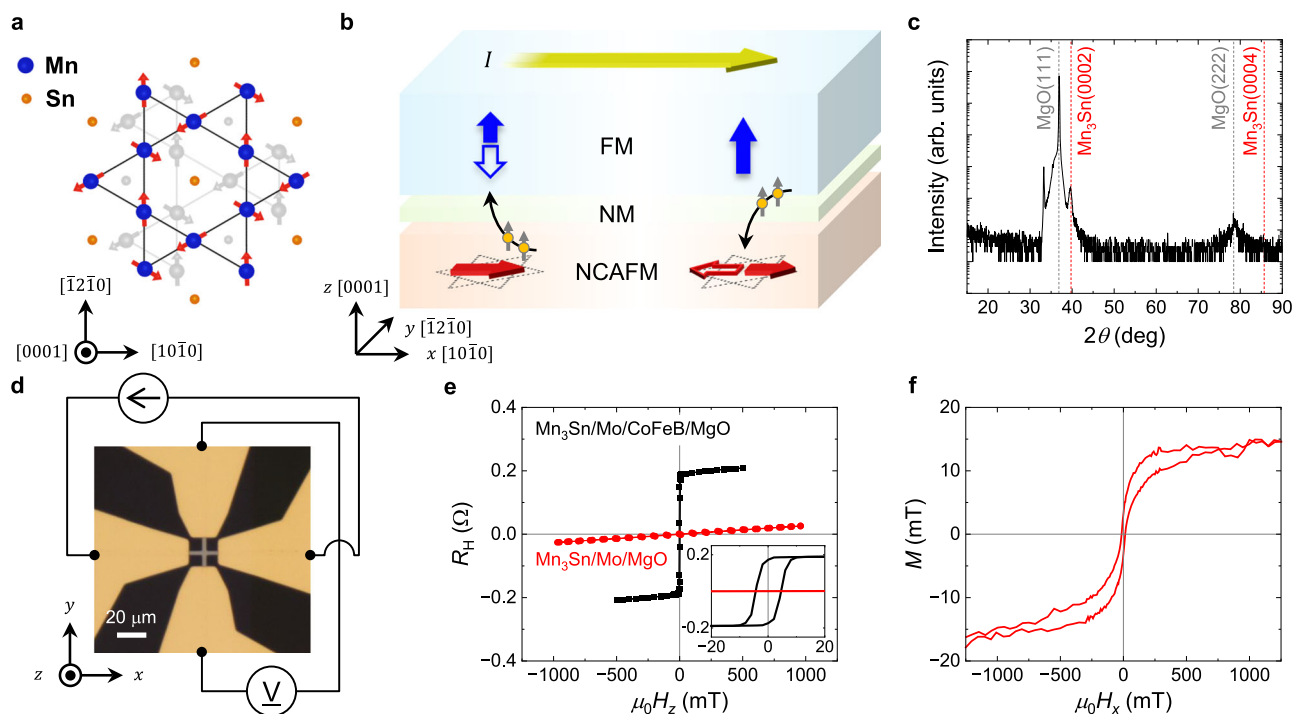

Fig. 1 | Structural, transport, and magnetic properties. a Atomic and chiral-spin structures in a kagome plane of the NCAFM $D0_{19}$-Mn$_3$Sn. The blurred color denotes the atoms and magnetic moments in the neighboring kagome plane. **b** Schematic of the electrical mutual switching in Mn$_3$Sn/Mo/CoFeB. Red, blue, and gray arrows denote the magnetic orientations of Mn$_3$Sn, CoFeB, and non-equilibrium spins with z-component, respectively. NM: nonmagnetic material. **c** Out-of-plane X-ray diffraction result in a Ru(2 nm)/Mn$_3$Sn(30 nm)/MgO(1.3 nm)/Ru(1 nm) stack. A large thickness of Mn$_3$Sn is used here in order to obtain clear signal. **d** Optical image of a Hall bar device, which is connected to a current source and a voltmeter for transport measurements. **e** R_H – H_z loops of Mn$_3$Sn/Mo/CoFeB/MgO (black) and Mn$_3$Sn/Mo/MgO (red). The inset shows the zoomed-in region around the switching of CoFeB. **f** Magnetization M as a function of the in-plane magnetic field $\mu_0 H_x$ in the same stack of (**c**).

triangle. The magnetic orientation of the chiral-spin structure can be represented by the magnetization vector (similarly, the octupole moment) and is controllable by magnetic fields[20].

The films are patterned to Hall bar devices (Fig. 1d) with which the magnetic states of CoFeB can be detected via the anomalous Hall effect (AHE)[30]. Meanwhile, because the AHE in Mn_3Sn appears in the transverse direction to the Berry curvature that arises in the kagome plane, the AHE voltage is not observable for the (0001)-oriented Mn_3Sn thin films[20]. Figure 1e shows the Hall resistance R_H under an out-of-plane magnetic field H_z. A sharp hysteresis loop with ~100% remanence is observed in Mn_3Sn/Mo/CoFeB/MgO, whereas a control sample of Mn_3Sn/Mo/MgO shows a linear background from the ordinary Hall effect. This comparison confirms that the jump of R_H corresponds to the switching of the perpendicularly magnetized CoFeB without any exchange coupling with Mn_3Sn layer (also see Supplementary Fig. 2 for the $M - H_x$ loop of Mn_3Sn/Mo/CoFeB/MgO). The reversal field of CoFeB is less than 10 mT.

The magnetic property of Mn_3Sn is characterized by the in-plane magnetic hysteresis loop in Fig. 1f. The remanence at zero field is ~20% of the saturation magnetization, which is consistent with previous studies on (0001)-oriented Mn_3Sn thin films[18,31,32] and suggests the multi-domain structure of our Mn_3Sn layer at zero magnetic field.

Polarity-reversible field-free switching of CoFeB by the MSHT from Mn_3Sn

The prerequisite of electrical mutual switching is to verify a reversible switching polarity of CoFeB by the MSHT from Mn_3Sn. In this section, we use a magnetic field to control the magnetic orientation (represented by the net magnetization vector) of the spin source Mn_3Sn. The measurement sequence is shown in Fig. 2a. We first initialize Mn_3Sn with $\mu_0 H_{AFM}^{init} = \pm 1$ T and then withdraw the field. Due to the multiple equivalent easy axes within the (0001) kagome plane[33], Mn_3Sn acquires a multi-domain state that maintains an overall preference of the magnetic orientation along the initialization field[34]. Next, CoFeB is

aligned by $\mu_0 H_{FM}^{init} = 0, \pm 40$ mT, followed by withdrawing the field. Subsequently, 100-ms pulse current is applied along the x direction with an in-plane magnetic field $\mu_0 H_x^{meas} = -10 \sim +10$ mT to perform the current-induced switching.

Here we focus on the results at $\mu_0 H_x^{meas} = 0$. Figure 2b, c show the $R_H - I$ loops of CoFeB switching (critical current density of ~ 9 MAcm^{-2}) after Mn_3Sn is initialized in the opposite directions $\pm x$. The field-free switching cannot be achieved by the weak spin Hall effect of Mo (Supplementary Fig. 3, also see refs. 35,36), but is consistent with the anti-damping MSHT switching via the z-component spins of Mn_3Sn. Remarkably, the switching polarity is reversed by flipping the magnetic orientation of Mn_3Sn (also see Supplementary Fig. 4a), in sharp contrast to the existing studies in which the field-free switching polarity is immune to the magnetic influence on the NCAFM[18,37]. We thus verify that the MSHE (that is, the $\pm z$ spin polarization is determined by the magnetic orientation of Mn_3Sn along $\pm x$) plays a critical role in the observed current-induced switching[19]. This is further supported by the absence of field-free switching when Mn_3Sn is initialized along $\pm y$ (Fig. 2d, e), in agreement with a spin-torque ferromagnetic resonance study in Mn_3Sn(0001)/NiFe bilayers[17] and theoretical calculations[16,18]. These results verify that Mn_3Sn can serve as a reversible magnetic spin source to induce polarity-controllable field-free switching of CoFeB via the MSHT.

As an additional note, while Mn_3Sn obtains a net magnetic orientation from $\mu_0 H_{AFM}^{init}$, it has a multi-domain structure after withdrawing the field. Taking the configuration of Fig. 2b as an example, under a positive current, the Mn_3Sn domains with $+x$ components provide the spins whose polarization is suitable to switch CoFeB from down to up, while other domains with $-x$ components provide opposite spins that do not support such switching. As a whole, we obtain a partially compensated MSHT and a reduced switching ratio of CoFeB containing unswitched domains (also see Supplementary Information). We also note that the intralayer spin-transfer torque in CoFeB, with the possibility of inducing
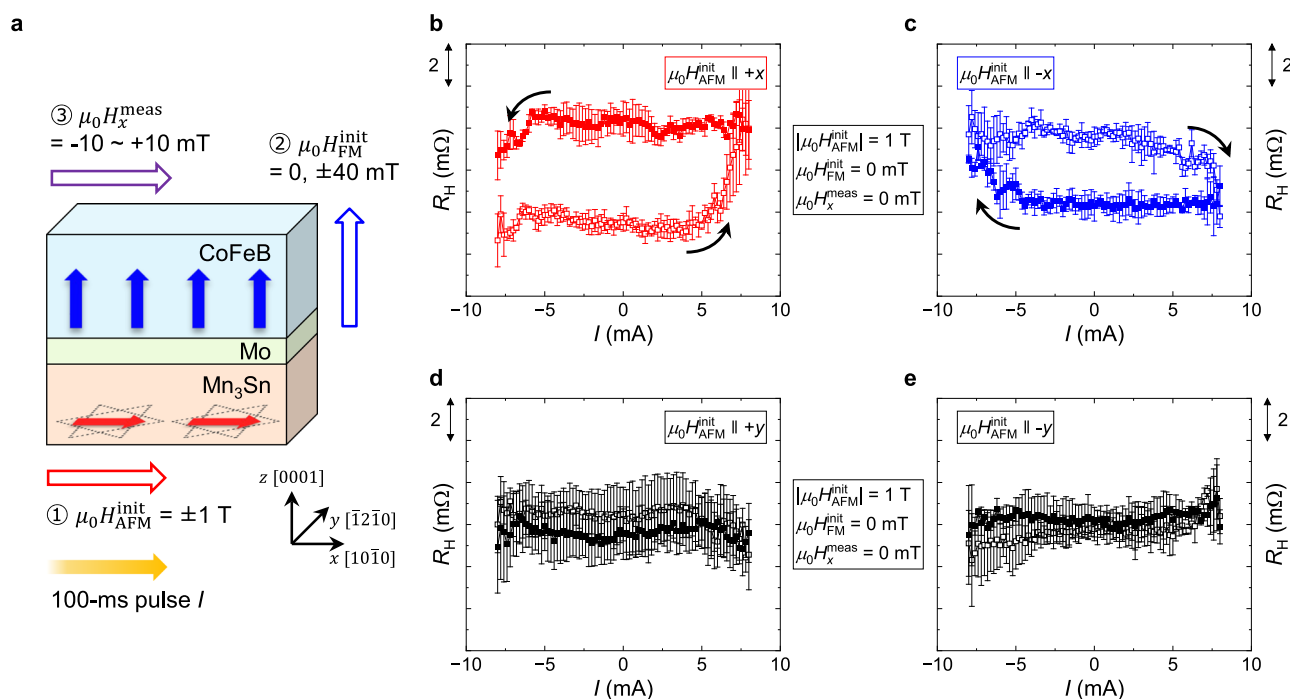

Fig. 2 | Switching of CoFeB by the MSHT of Mn_3Sn. a Sequence of the switching measurements. H_{AFM}^{init}, H_{FM}^{init}, and H_x^{meas} are the AFM initialization field, FM initialization field, and the field applied during the measurement, respectively. 100-ms pulse current is applied to induce the switching. Field-free switching of CoFeB. The

magnetic spin source Mn_3Sn is initialized by a magnetic field of 1 T along (**b**) +x, (**c**) -x, (**d**) +y, and (**e**) -y directions, respectively. Open (closed) symbols indicate the data plots during the forward (backward) scan. The error bars indicate the standard deviation errors in three continuous rounds of measurements.
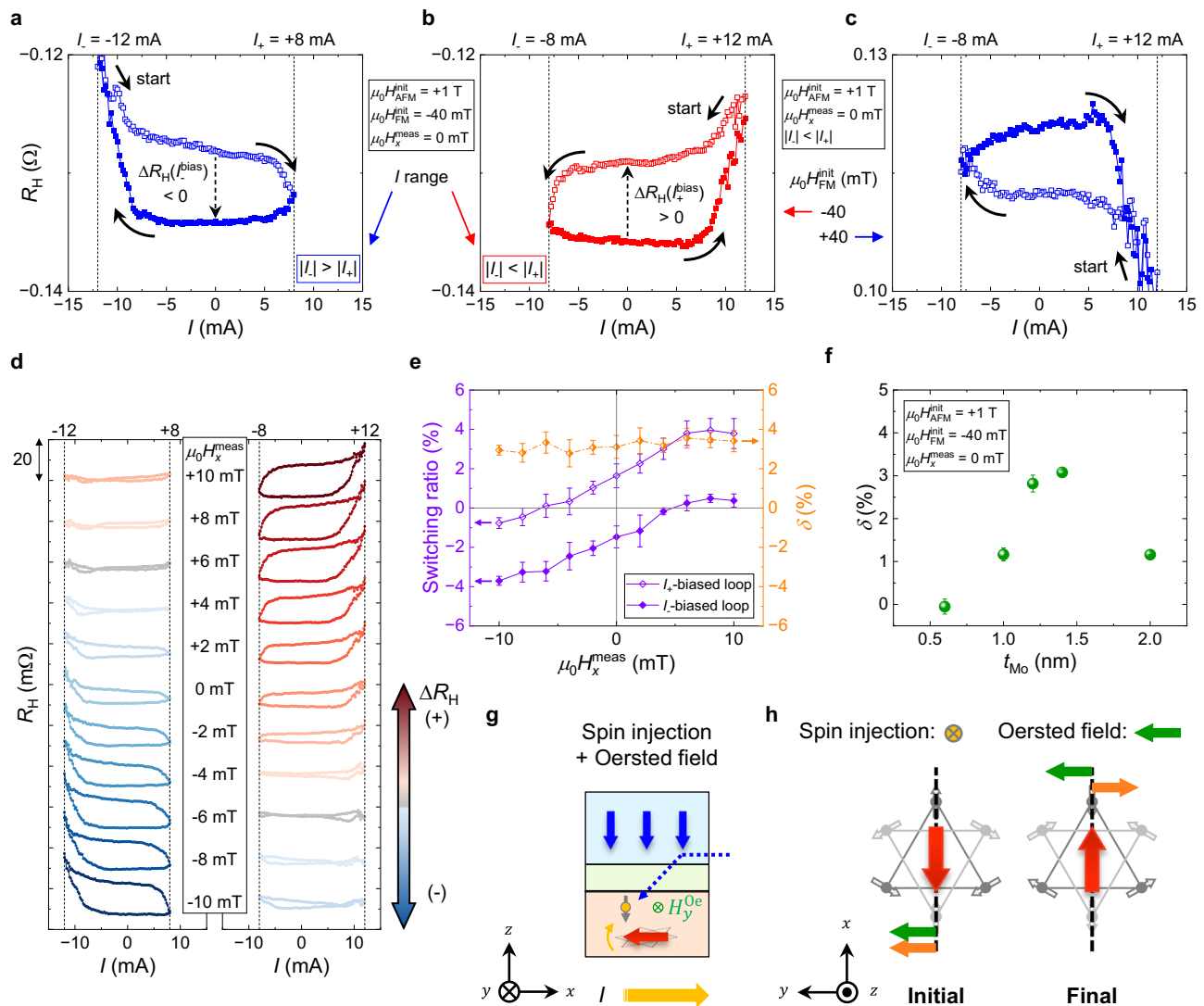
Fig. 3 | Electric control of the MSHT via switching Mn₃Sn. a–c $R_H - I$ measurements performed in various conditions. Shared conditions of neighboring figures are shown in a legend between the figures. Current range dependence of R_H, where the absolute value of the maximum current at positive side, I_+ is smaller (larger) than that of the minimum current at negative side, I_- in (**a**, **b**). CoFeB initialization dependence of R_H, where CoFeB is initialized along $-z$ ($+z$) in (**b**, **c**). **d** In-plane magnetic field $\mu_0 H_x^{meas}$ dependence of I_--biased (left) and I_+-biased (right) loops. $\mu_0 H_x^{meas}$ varies from -10 to $+10$ mT with a step of 2 mT. The switching magnitude ΔR_H is qualitatively described by a scaling arrow with a colored gradient.

e Switching ratio of the loops shown in (**d**) and the difference δ between I_--biased and I_+-biased loops. **f** t_{Mo} dependence of δ at zero magnetic field. The error bars in (**e**, **f**) indicate the standard deviation errors in five continuous rounds of measurements. **g** Key factors of the Mn₃Sn switching, where H_y^{Oe} is an Oersted field along y direction. **h** Schematic for the switching process of Mn₃Sn. Red arrows indicate the net magnetization representing the overall magnetic order of Mn₃Sn. Orange arrows denote the effective rotation direction of the net magnetization of Mn₃Sn under spin injection. Green arrows denote the rotation of the net magnetization of Mn₃Sn driven by the Oersted field.

domain wall motion, cannot explain our experimental results in Fig. 2b–e, which, otherwise, should not depend on the initialization along $\pm x$ and $\pm y$. To be seen in the next section, similar arguments apply to exclude the spin-transfer torque within Mn₃Sn according to Fig. 3b, c. Moreover, the larger bias current in Fig. 3a should not be attributed to the critical current for the spin-transfer torque-induced domain wall motion, because a smaller current in the opposite direction also triggers the switching of CoFeB.

Electrical control of the MSHT polarity from the magnetic spin source Mn₃Sn

The subsequent step towards the electrical mutual switching is to use electric current, instead of magnetic field, to set the magnetic orientation of Mn₃Sn. We find that it can be achieved in the same device using the polarized spin current flowing from CoFeB to Mn₃Sn, where the critical treatment is just to apply a larger current as a bias at the

beginning. Figure 3a, b show the $R_H - I$ loops, where the electric current is applied in the range of -12 mA $\leq I \leq +8$ mA and -8 mA $\leq I \leq +12$ mA, respectively, in the absence of magnetic field. We call the former (latter) an $I_-(I_+)$-biased loop. Notably, opposite polarities of the MSHT-induced CoFeB switching are obtained only by changing the bias current direction. Given that the switching polarity is determined by the magnetic orientation of the spin source Mn₃Sn (verified by the measurements with a symmetric current range of -8 mA $\leq I \leq +8$ mA in Fig. 2b, c), the observed phenomena indicate that Mn₃Sn is switched in the large current regime of $|I| > 8$ mA (also see Supplementary Fig. 4b).

To elucidate the field-free switching of Mn₃Sn, we first figure out the role of the CoFeB layer. Figure 3b, c show the polarity dependence of the CoFeB switching on the CoFeB initialization along $-z$ and $+z$, respectively (indicated by the sign of R_H). We can see that the opposite switching polarities are correlated to the different initialization directions of CoFeB (Supplementary Fig. 4b). Given that the switching

polarity is determined by the magnetic orientation of Mn$_3$Sn, this result indicates that CoFeB, while playing a traditional role as the target magnetic electrode being switched, also works as a magnetic spin source to switch Mn$_3$Sn. As a consequence, the intrinsic SOT polarity of the CoFeB switching from Mn$_3$Sn becomes programmable by current. Thermal effects such as demagnetization and magnetoelastic effect cannot explain the dependence of CoFeB on the bias current or CoFeB initialization (see Supplementary Information).

We then investigate the influence of in-plane magnetic fields on the Mn$_3$Sn switching. Figure 3d shows the H_x^{meas} dependence of $R_H - I$ loops in I_--biased (left) and I_+-biased (right) regimes. Figure 3e summarizes the switching ratio defined as $\Delta R_H\left(I_{+(-)}^{\text{bias}}\right)/R_H^0$, where $\Delta R_H\left(I_{+(-)}^{\text{bias}}\right)$ and R_H^0 are the magnitudes of CoFeB switching in the I_+ (I_-)-biased loop (dashed arrows in Fig. 3a, b) and the $R_H - H_z$ loop (Fig. 1e), respectively. The switching ratio varies from −1% to +4% for I_+-biased loop and −4% to +1% for I_--biased loop with a constant difference δ of ~3%. δ by definition represents the portion of Mn$_3$Sn domains that are oriented by the bias current rather than H_x^{meas}. The monotonic variation of the switching ratio can be attributed to the Mn$_3$Sn domains that are gradually oriented as the external magnetic field H_x^{meas} increases, which is illustrated in Supplementary Fig. 5. On the other hand, the switching ratio is suppressed by the constant magnetic field along y (H_y^{meas}), as the y-oriented Mn$_3$Sn domains do not facilitate the MSHT switching[17]. Figure 3f shows t_{Mo} dependence of δ at zero magnetic field, which increases with t_{Mo} in the region of $0.6\,\text{nm} \leq t_{\text{Mo}} \leq 1.4\,\text{nm}$ and decreases back at $t_{\text{Mo}} = 2\,\text{nm}$. This result implies that Mn$_3$Sn can be manipulated only when t_{Mo} is larger than a threshold (0.6 nm), and the effect decreases after a certain value of t_{Mo}.

Here we propose a possible mechanism of Mn$_3$Sn switching to consistently explain the observations above. Previous studies showed that both spin injection and external magnetic field are indispensable for the current-induced switching in Mn$_3$Sn/heavy metal bilayers[38–44]. In our case, the switching of Mn$_3$Sn can be attributed to the combined effect of the sign-fixed z-oriented spins polarized by the perpendicularly magnetized CoFeB and the sign-flippable y-oriented Oersted field from the electric current (Fig. 3g, h, also see Supplementary Information). The z-oriented spins in Fig. 3g are polarized by the perpendicular magnetization of CoFeB, similar to the spin transfer in current-in-plane spin valves[25]. These spins do not flip sign when the current is reversed. As a result, the switching mechanism in Fig. 3h (demonstrated in ref. 44) can work in our system if Mn$_3$Sn contains certain domains with an easy axis along x (refs. 41,44), which is possible under current-induced effects[45]. Moreover, the magnitudes of the Oersted field and the injected z-oriented spins scale in the opposite way as t_{Mo} increases (Supplementary Fig. 6), which can explain the observed non-monotonic t_{Mo} dependence of δ in Fig. 3f. We notice the different switching behaviors in the $t_{\text{Mo}} = 0.6\,\text{nm}$ sample compared to those of $t_{\text{Mo}} \geq 1.2\,\text{nm}$ samples in terms of no field-free switching and the opposite switching polarities, which can be interpreted by the randomly oriented Mn$_3$Sn domains due to the chiral-spin rotation[39] that appears in the samples with a very thin Mo layer (also see Supplementary Figs. 6b and 7). We have also examined other scenarios by considering the stray field from CoFeB and the non-equilibrium spins from various mechanisms in CoFeB (ref. 25) and Mo (refs. 35,36) bulks as well as at the Mo/CoFeB interface[25,46]. However, as detailed in Supplementary Table 1, all the other scenarios cannot describe the observed Mn$_3$Sn switching.

Full sequence of the electrical mutual switching

After studying the field-free switching of CoFeB and of Mn$_3$Sn separately, we provide in Fig. 4a a full sequence of the electrical mutual switching in a wider current range of $-12\,\text{mA} \leq I \leq +12\,\text{mA}$. The unchanged sign of R_H during the current scan indicates the existence of unswitched CoFeB domains, which is essential for the repeatable mutual switching (otherwise, demagnetization of both magnetic layers will occur in the large current regime). Figure 4b sketches a self-consistent qualitative model of the critical steps in Fig. 4a. Steps (A) to (E) ((F) to (J)) show the forward (backward) process with the electric
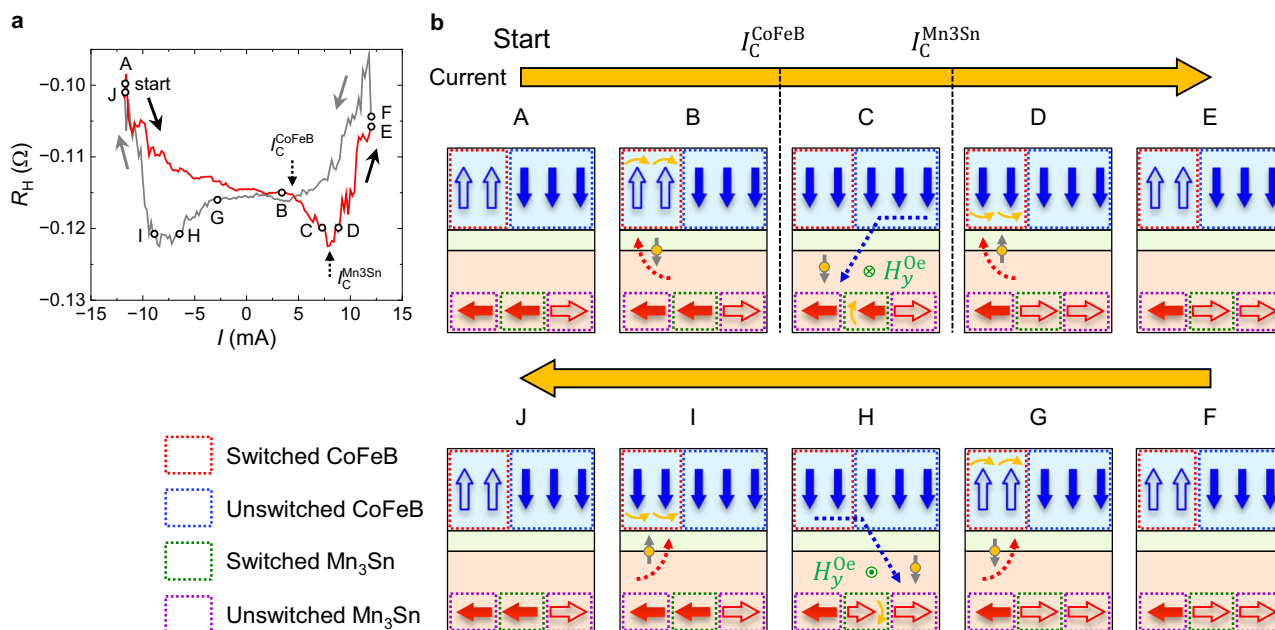

Fig. 4 | Full sequence of the electrical mutual switching in Mn$_3$Sn/Mo/CoFeB. a Full $R_H - I$ loop measured in the range of $-12\,\text{mA} \leq I \leq +12\,\text{mA}$ without external magnetic fields. $I_C^{\text{CoFeB(Mn3Sn)}}$ denotes the critical current for switching CoFeB (Mn$_3$Sn). Mn$_3$Sn and CoFeB are initialized along $+x$ and $-z$ directions by magnetic fields, respectively. **b** Schematics for the electrical mutual switching between CoFeB and Mn$_3$Sn. Panels (**A**–**J**) correspond to the states labeled in (**a**). Red (blue) and green (purple) dashed rectangles indicate the switched (unswitched) CoFeB domains and the switched (unswitched) Mn$_3$Sn domains, respectively. The blue-boxed unswitched CoFeB domains exist on top of the multi-domain structure of Mn$_3$Sn. Dashed arrows indicate the spin flow pointing from its origin to the target. Yellow curved arrows illustrate the torque acting on the target magnetic moments.
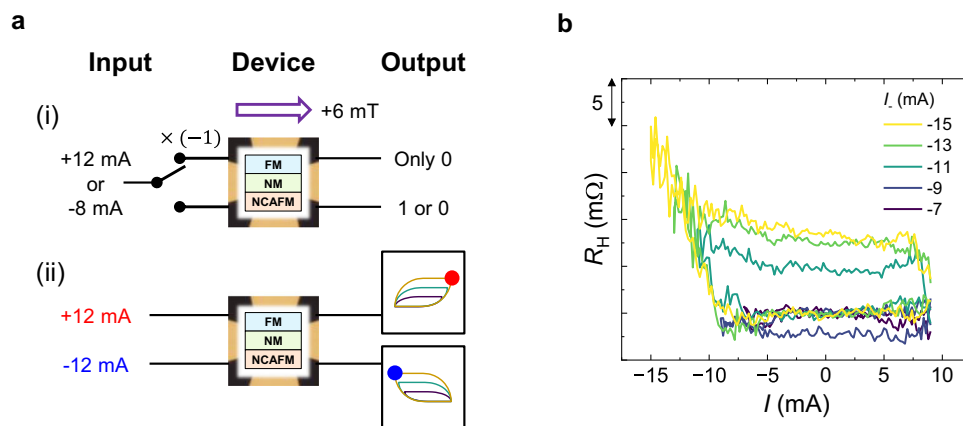
Fig. 5 | Proof-of-concept device functionalities. a Illustration of the functionalities of electrically programmable logic (i) and memristive switching (ii). **b** $R_H - I$ loops with various I_- and fixed I_+ of +8 mA in the absence of external magnetic fields.

current increasing (decreasing) from −12 mA to +12 mA (+12 mA to −12 mA) (A) Magnetic states are set by $I = -12$ mA, where CoFeB is dominated by −z-oriented domains and the net magnetic orientation of Mn₃Sn is switched to −x. (B) Certain CoFeB domains, marked by the red dashed rectangles in Fig. 4b, start to be switched by the MSHT from Mn₃Sn. (C) Beyond the critical current I_C^{CoFeB}, CoFeB has already been switched and the reversible Mn₃Sn domain in the green dashed rectangle starts to undergo the mechanism in Fig. 3g due to CoFeB dominantly oriented along −z. (D, E) Beyond another larger critical current I_C^{Mn3Sn}, Mn₃Sn is switched, so that the net MSHT from Mn₃Sn reverses its polarity and further switches CoFeB. The backward steps of (F) to (J) can be understood in a similar way. Since the magnetic domains are randomly dispersed in Mn₃Sn and CoFeB, the ensemble effect throughout the film is a reduced magnitude of CoFeB switching (see Supplementary Information). We note that this multi-domain model, supported by magnetic measurements (Fig. 1f and Supplementary Fig. 8), provides a reasonable explanation of our experimental results. Further increasing the switching ratio can be potentially achieved by enhancing the x-axis uniaxial anisotropy of Mn₃Sn or reducing the switching barrier of CoFeB.

Proof-of-concept device functionalities

The electrical mutual switching triggers intriguing functionalities in logic and computing. First, it enables selective turning on and off for the switching process by current. The Mn₃Sn domains contributing to the CoFeB switching can be controlled by the electric current and the magnetic field independently as represented in Fig. 3e. Therefore, by tuning the in-plane magnetic field $\mu_0 H_x^{meas}$ (e.g., ±6 mT in Fig. 3d) to enlarge or reduce the Mn₃Sn domains in a typical orientation, the switching process can be precisely turned on and off. Such a controllable switching process (output) by reversing the sign of the input current can be used to design SOT-based logic devices (Fig. 5a (i)).

Another unique application of our electrical mutual switching lies in the neuromorphic computing built on memristive behaviors, where the amount of past electric charge is memorized in its magnetic states[5,7]. Such behaviors are manifested by the multistep magnetic switching in our device. As plotted in Fig. 5b, the switching magnitude is determined in an analogue way by the magnitude of the applied current. This multistep switching is caused by the nucleation and expansion of Mn₃Sn domains dispersed in the film (a common phenomenon in the switching of antiferromagnets[34,47,48]), which determines the switching of CoFeB via the MSHT (Supplementary Fig. 9). Strikingly, our mutual switching allows one to electrically reverse the polarity of the memristive transition (output) by the bias current direction (input) (Fig. 3a, b, also illustrated in Fig. 5a (ii)). It provides an extra tuning knob for the build blocks of neuromorphic computing, in contrast to the existing schemes whose polarity cannot be electrically programmed[7,49].

In summary, we show a proof-of-concept current-induced mutual switching between a NCAFM and a FM, using a spin-valve-like simple protocol consisting of Mn₃Sn/Mo/CoFeB. The spin current to switch one magnetic layer arises from the interactions between the intrinsic magnetic structure and the electric current in the other magnetic layer, which is the key to the mutual switching. Particularly, it allows us to control the polarity of the CoFeB switching by electrically flipping the magnetic orientation of Mn₃Sn. This distinct switching scheme gives rise to electrically programmable logic and computing functions, paving a way towards innovative spintronic devices.

Methods

Sample preparation

Stacks of Ru(2 nm)/Mn₃Sn(30 nm)/MgO(1.3 nm)/Ru(1 nm) were deposited by DC/RF magnetron sputtering on MgO(111) single crystal substrates. Ru and Mn₃Sn were deposited at 450 °C and MgO was deposited at room temperature. The deposition was implemented under the base pressure of less than 1×10^{-6} Pa. Subsequently, samples were annealed at 500 °C for 1 h in vacuum. After annealing, capping layers of MgO/Ru and a part of Mn₃Sn layer were etched by bias-sputtering, with 17 nm thick Mn₃Sn left, followed by depositing Mo(t_{Mo})/CoFeB(1 nm)/MgO(1.3 nm)/TaO$_x$(1 nm) at room temperature. The Mo thickness t_{Mo} varied as 0.6, 1.0, 1.2, 1.4, and 2.0 nm. To obtain a perpendicular magnetic easy axis of CoFeB, the stacks were annealed at 300 °C for 1 h in vacuum. The stacks were fabricated into Hall bars by photolithography with channel width and length being 3 and 20 μm, respectively. Finally, contact pads consisting of Cr(5 nm)/Au(100 nm) were fabricated by standard photolithography and lift-off procedures.

X-ray diffraction

A Cu-Kα1 X-ray with a wavelength of 1.54056 Å was used in our X-ray diffraction measurements on a Bruker X-ray diffractometer.

Transport measurements

Transport measurements were performed on Hall bar devices via the four-probe method shown in Fig. 1d. All the transport measurements except the t_{Mo} dependence used a stack consisting of MgO(111) substrate/Ru(2 nm)/Mn₃Sn(17 nm)/Mo(1.4 nm)/CoFeB(1 nm)/MgO(1.3 nm)/TaO$_x$(1 nm). In the switching measurements, current pulses with a duration of 100 ms were applied to induce the switching, followed by a constant current of 0.5 mA to measure the Hall voltage.

Data availability

All data supporting the findings of this study are included within the main text or Supplementary Information and are also available from the corresponding authors upon reasonable request.

References

1. Miron, I. M. et al. Perpendicular switching of a single ferromagnetic layer induced by in-plane current injection. *Nature* **476**, 189–193 (2011).

2. Liu, L. et al. Spin-torque switching with the giant spin Hall effect of tantalum. *Science* **336**, 555–558 (2012).

3. Fukami, S., Anekawa, T., Zhang, C. & Ohno, H. A spin–orbit torque switching scheme with collinear magnetic easy axis and current configuration. *Nat. Nanotechnol.* **11**, 621–625 (2016).

4. Manchon, A. et al. Current-induced spin-orbit torques in ferromagnetic and antiferromagnetic systems. *Rev. Mod. Phys.* **91**, 035004 (2019).

5. Shao, Q. et al. Roadmap of spin–orbit torques. *IEEE Trans. Magn.* **57**, 1–39 (2021).

6. Natsui, M. et al. Dual-port SOT-MRAM achieving 90-MHz read and 60-MHz write operations under field-assistance-free condition. *IEEE J. Solid-State Circuits* **56**, 1116–1128 (2021).

7. Fukami, S., Zhang, C., DuttaGupta, S., Kurenkov, A. & Ohno, H. Magnetization switching by spin–orbit torque in an antiferromagnet–ferromagnet bilayer system. *Nat. Mater.* **15**, 535–541 (2016).

8. Lau, Y.-C., Betto, D., Rode, K., Coey, J. M. D. & Stamenov, P. Spin–orbit torque switching without an external field using interlayer exchange coupling. *Nat. Nanotechnol.* **11**, 758–762 (2016).

9. Baek, S. C. et al. Spin currents and spin–orbit torques in ferromagnetic trilayers. *Nat. Mater.* **17**, 509–513 (2018).

10. Lin, P.-H. et al. Manipulating exchange bias by spin–orbit torque. *Nat. Mater.* **18**, 335–341 (2019).

11. Peng, S. et al. Exchange bias switching in an antiferromagnet/ferromagnet bilayer driven by spin–orbit torque. *Nat. Electron.* **3**, 757–764 (2020).

12. Cai, K. et al. Electric field control of deterministic current-induced magnetization switching in a hybrid ferromagnetic/ferroelectric structure. *Nat. Mater.* **16**, 712–716 (2017).

13. Chen, X. et al. Electric field control of Néel spin–orbit torque in an antiferromagnet. *Nat. Mater.* **18**, 931–935 (2019).

14. Yan, H. et al. A piezoelectric, strain-controlled antiferromagnetic memory insensitive to magnetic fields. *Nat. Nanotechnol.* **14**, 131–136 (2019).

15. Filianina, M. et al. Electric-field control of spin–orbit torques in perpendicularly magnetized W/CoFeB/MgO films. *Phys. Rev. Lett.* **124**, 217701 (2020).

16. Kimata, M. et al. Magnetic and magnetic inverse spin Hall effects in a non-collinear antiferromagnet. *Nature* **565**, 627–630 (2019).

17. Kondou, K. et al. Giant field-like torque by the out-of-plane magnetic spin Hall effect in a topological antiferromagnet. *Nat. Commun.* **12**, 6491 (2021).

18. Hu, S. et al. Efficient perpendicular magnetization switching by a magnetic spin Hall effect in a noncollinear antiferromagnet. *Nat. Commun.* **13**, 4447 (2022).

19. Cao, C. et al. Anomalous spin current anisotropy in a noncollinear antiferromagnet. *Nat. Commun.* **14**, 5873 (2023).

20. Nakatsuji, S., Kiyohara, N. & Higo, T. Large anomalous Hall effect in a non-collinear antiferromagnet at room temperature. *Nature* **527**, 212–215 (2015).

21. Qin, P. et al. Room-temperature magnetoresistance in an all-antiferromagnetic tunnel junction. *Nature* **613**, 485–489 (2023).

22. Chen, X. et al. Octupole-driven magnetoresistance in an antiferromagnetic tunnel junction. *Nature* **613**, 490–495 (2023).

23. Chen, X. et al. Observation of the antiferromagnetic spin Hall effect. *Nat. Mater.* **20**, 800–804 (2021).

24. Nan, T. et al. Controlling spin current polarization through non-collinear antiferromagnetism. *Nat. Commun.* **11**, 4671 (2020).

25. Fert, A. Nobel Lecture: Origin, development, and future of spintronics. *Rev. Mod. Phys.* **80**, 1517–1530 (2008).

26. Yu, G. et al. Switching of perpendicular magnetization by spin–orbit torques in the absence of external magnetic fields. *Nat. Nanotechnol.* **9**, 548–554 (2014).

27. You, L. et al. Switching of perpendicularly polarized nanomagnets with spin orbit torque without an external magnetic field by engineering a tilted anisotropy. *Proc. Natl Acad. Sci. USA* **112**, 10310–10315 (2015).

28. Ikeda, S. et al. A perpendicular-anisotropy CoFeB–MgO magnetic tunnel junction. *Nat. Mater.* **9**, 721–724 (2010).

29. Yoon, J. et al. Crystal orientation and anomalous Hall effect of sputter-deposited non-collinear antiferromagnetic Mn$_3$Sn thin films. *Appl. Phys. Express* **13**, 013001 (2019).

30. Nagaosa, N., Sinova, J., Onoda, S., MacDonald, A. H. & Ong, N. P. Anomalous Hall effect. *Rev. Mod. Phys.* **82**, 1539–1592 (2010).

31. Hazra, B. K. et al. Generation of out-of-plane polarized spin current by spin swapping. *Nat. Commun.* **14**, 4549 (2023).

32. Markou, A. et al. Noncollinear antiferromagnetic Mn$_3$Sn films. *Phys. Rev. Mater.* **2**, 051001 (2018).

33. Duan, T. F. et al. Magnetic anisotropy of single-crystalline Mn$_3$Sn in triangular and helix-phase states. *Appl. Phys. Lett.* **107**, 082403 (2015).

34. Uchimura, T. et al. Observation of domain structure in non-collinear antiferromagnetic Mn$_3$Sn thin films by magneto-optical Kerr effect. *Appl. Phys. Lett.* **120**, 172405 (2022).

35. Sinova, J., Valenzuela, S. O., Wunderlich, J., Back, C. H. & Jungwirth, T. Spin Hall effects. *Rev. Mod. Phys.* **87**, 1213–1260 (2015).

36. Mosendz, O. et al. Quantifying spin Hall angles from spin pumping: experiments and theory. *Phys. Rev. Lett.* **104**, 046601 (2010).

37. Han, R. K. et al. Field-free magnetization switching in CoPt induced by noncollinear antiferromagnetic Mn$_3$Ga. *Phys. Rev. B* **107**, 134422 (2023).

38. Tsai, H. et al. Electrical manipulation of a topological antiferromagnetic state. *Nature* **580**, 608–613 (2020).

39. Takeuchi, Y. et al. Chiral-spin rotation of non-collinear antiferromagnet by spin–orbit torque. *Nat. Mater.* **20**, 1364–1370 (2021).

40. Yan, G. Q. et al. Quantum sensing and imaging of spin–orbit-torque-driven spin dynamics in the non-collinear antiferromagnet Mn$_3$Sn. *Adv. Mater.* **34**, 2200327 (2022).

41. Higo, T. et al. Perpendicular full switching of chiral antiferromagnetic order by current. *Nature* **607**, 474–479 (2022).

42. Krishnaswamy, G. K. et al. Time-dependent multistate switching of topological antiferromagnetic order in Mn$_3$Sn. *Phys. Rev. Appl.* **18**, 024064 (2022).

43. Pal, B. et al. Setting of the magnetic structure of chiral kagome antiferromagnets by a seeded spin-orbit torque. *Sci. Adv.* **8**, eabo5930 (2022).

44. Yoon, J.-Y. et al. Handedness anomaly in a non-collinear antiferromagnet under spin–orbit torque. *Nat. Mater.* **22**, 1106–1113 (2023).

45. Zhang, P., Finley, J., Safi, T. & Liu, L. Quantitative study on current-induced effect in an antiferromagnet insulator/Pt bilayer film. *Phys. Rev. Lett.* **123**, 247206 (2019).

46. Amin, V. P., Zemen, J. & Stiles, M. D. Interface-generated spin currents. *Phys. Rev. Lett.* **121**, 136805 (2018).

47. Li, S. et al. Nanoscale magnetic domains in polycrystalline Mn$_3$Sn films imaged by a scanning single-spin magnetometer. *Nano Lett.* **23**, 5326–5333 (2023).

48. Baldrati, L. et al. Mechanism of Néel order switching in antiferromagnetic thin films revealed by magnetotransport and direct imaging. *Phys. Rev. Lett.* **123**, 177201 (2019).

49. Krishnaswamy, G. et al. Multidomain memristive switching of Pt$_{38}$Mn$_{62}$/[Co/Ni]$_n$ multilayers. *Phys. Rev. Appl.* **14**, 044036 (2020).

Acknowledgements

Author contributions
J.-Y.Y., R.T., J.H., and S.F. planned the study. J.-Y.Y., Y.T., and R.T. designed the stacks. J.-Y.Y., R.T., and T.U. prepared the stacks. J.-Y.Y. characterized the basic properties of the stacks. J.-Y.Y. and R.T. fabricated the stack into the devices. J.-Y.Y. performed transport measurements and analysed the data with input from Y.T., R.T., Y.Y., J.I., and S.F. All authors discussed the results. J.-Y.Y., J.H., and S.F. wrote the manuscript with input from the other authors. H.O. and S.F. supervised the research.

Competing interests
The authors declare no competing interests.

Additional information
Supplementary information The online version contains supplementary material available at https://doi.org/10.1038/s41467-025-56157-6.

Correspondence and requests for materials should be addressed to Jiahao Han or Shunsuke Fukami.

Peer review information *Nature Communications* thanks the anonymous reviewer(s) for their contribution to the peer review of this work. A peer review file is available.

Reprints and permissions information is available at http://www.nature.com/reprints

Publisher's note Springer Nature remains neutral with regard to jurisdictional claims in published maps and institutional affiliations.